Article

Iceberg-like pyramids in industrially textured silicon enabled 33% efficient perovskite-silicon tandem solar cells

Daoyong Zhang[1,4], Tao Wu[2,4], Biao Li[1], Degong Ding[1], Ruilin Li[1], Jiyao Wei[1], Hengyu Zhang[1], Chenxia Kan[1], Yuxin Yao[1], Pengjie Hang[1]✉, Zhiguo Yu[1,3], Zhenyi Ni[1], Kaifu Qiu[2], Deren Yang[1,3]✉ & Xuegong Yu[1,3]✉

The pursuit of higher-efficiency solar cells has spurred the integration of perovskite materials with silicon-based technologies, yet achieving an efficient tandem architecture that leverages industrially textured silicon (ITS) with pyramid sizes larger than 2 μm remains a significant challenge. Such textured surfaces complicate the uniform coverage of the subsequent hole-selective layer deposition and the high-quality deposition of perovskites, ultimately causing significant contact losses in tandem devices. This study presents a tandem solar cell architecture that employs localized submicron contacts, enabled by silica (SiO_X) nanospheres, to effectively regulate silicon substrate surfaces that exhibit iceberg-like pyramids. This architecture facilitates the complete coverage of solution-processed perovskites on ITS substrates while substantially reducing interfacial recombination losses and enhancing charge carrier transport. Consequently, the developed tandem solar cells demonstrate certified power conversion efficiencies of up to 33.15% in a one square centimeter area, along with improved device stability.

Perovskite-based solar cells have shown remarkable progress in recent years[1,2], particularly in the integration with silicon solar cells to form a tandem architecture, which presents a promising avenue for enhancing solar cell efficiency while reducing manufacturing costs[3,4]. Recent advancements have demonstrated monolithic perovskite-silicon tandem solar cells achieving power conversion efficiencies (PCEs) exceeding 32% using polished or submicron textured silicon (STS) substrates[5–8]. These optimized silicon bottom cells enable nearly conformal growth of hole selective layers followed by high-crystallinity, solution-processed perovskite layers, resulting in the peak efficiency value of 34.6% reported by LONGi[1].

However, while tandems with optimized silicon substrates have demonstrated high efficiencies, they are not compatible with standard photovoltaic manufacturing processes, which limits their production capacity and economic viability[9,10]. In contrast, industrially textured silicon (ITS), featuring micron-sized (~2 μm) pyramids, offers a more attractive and cost-effective solution[11–13]. These substrates can be produced directly within existing silicon cell manufacturing processes, ensuring scalability and compatibility with established industrial practices. Additionally, the industrially textured surface enhances light trapping, potentially improving the efficiency of tandem solar cells. Nonetheless, the industrially texturing introduces significant challenges for the full-coverage deposition of self-assembled monolayers (SAMs) on indium tin oxide (ITO) recombination layers. Areas where SAMs fail to anchor can lead to direct perovskite contacts with ITO, resulting in increased interfacial recombination losses[14,15]. Additionally, the deposition of perovskites on these textured substrates often requires a hybrid dry-wet method, which involves sequentially

[1]State Key Laboratory of Silicon and Advanced Semiconductor Materials and School of Materials Science & Engineering, Zhejiang University, Hangzhou, China. [2]Zhejiang Aiko Solar Energy Technology Co., Ltd, Yiwu, China. [3]Institute of Information and Functional Materials, ZJU-Hangzhou Global Scientific and Technological Innovation Center, Hangzhou, China. [4]These authors contributed equally: Daoyong Zhang, Tao Wu. ✉e-mail: hangpengjie@zju.edu.cn; mseyang@zju.edu.cn; yuxuegong@zju.edu.cn

depositing a halide framework followed by soaking in organic cation solutions[10,16,17]. Although this approach can improve the conformality of perovskite layers, essential for maximizing light trapping, it frequently compromises perovskite crystal quality relative to single-step solution deposition methods[11,18,19]. The textured surfaces of the perovskites can also complicate surface passivation[5,7,8,10], further hindering the overall performance. This underscores the importance of a quasi-planar surface design for silicon substrates that maintains effective light trapping.

Incorporating insulated passivation layers such as alumina (Al_2O_3) or poly(methyl methacrylate) (PMMA) to form nanoscale localized or tunneling contacts can effectively reduce interfacial recombination without impeding carrier transport, thereby enhancing solar cell efficiencies[20,21]. Given the structure of the textured silicon surface, our targeted design of localized submicron contacts represents a significant advancement for tandem architecture. By strategically filling the valleys of silicon pyramids with SiO_X nanospheres, we can achieve iceberg-like pyramids at the ITS surfaces, which not only improve the coverage of SAMs but also facilitate more effective perovskite deposition. This localized configuration enables precise electrical connectivity while leveraging the high light transmittance and anti-reflection properties of SiO_X nanospheres to maintain the benefits of light trapping. Consequently, we optimized the tandem solar cell performance, achieving a certified efficiency of 33.15%, the highest reported to date for monolithic perovskite-silicon tandem solar cells utilizing ITS. Notably, we found that the buried interface of perovskites at bottom of pyramid valleys was strengthened in the tandems, demonstrating superior stability compared to tandems with STS. This approach positions our tandem solar cells as a promising solution for the next generation of photovoltaic technologies.

Results

Construction of localized submicron contacts on ITS substrates

A high surface coverage of SAMs on transparent conductive oxides is crucial for reducing interfacial losses at the buried perovskite surface[14,22]. However, achieving this on highly rough substrates, especially ITS substrates with pyramid sizes up to approximately 2.5 μm in height—as confirmed by atomic force microscopy (AFM) and scanning electron microscopy (SEM) images in Fig. S1 is challenging. These surface textures require the perovskite layer to exceed 2 μm in thickness if deposited directly on the textured substrate, which however, impose substantial difficulties[23] for solution-processed perovskite deposition as it offers relatively poor conformality despite its advantages in producing high-quality perovskite layers compared to other techniques like the dry-wet hybrid process.

In this regard, we were motivated to address these deep textural features with an alternative strategy by introducing a pre-deposited layer, which could facilitate a flatter surface for the deposition of solution-processed high-quality perovskites, and simultaneously construct effective contacts for charge carrier transport. To achieve this, the pre-deposited layer should be capable of filling the deep valleys of the pyramid, highly transparent or even anti-reflective in optics to preserve the light trapping benefits of the deeply textured surfaces, and inert in charge conduction to minimize any undesired carrier recombination. In this context, we have ultimately opted for SiO_X nanospheres as the dielectric material, in contrast to more commonly used options such as Al_2O_3 or PMMA (see Fig. S2). This choice is predicated on the ability of SiO_X to effectively settle into the pyramid valleys of the textured silicon surface during the spin-coating process, as illustrated in Fig. 1a. Here, we tested the filling process using SiO_X nanospheres of varying sizes (20, 100, 200, and 500 nm). The final filling morphologies are shown in Figs. 1b, S3, and S4. We found that 100 nm SiO_X nanospheres exhibit filling efficacy comparable to 200 nm ones, whereas 20 nm particles poorly fill the valleys, forming irregular aggregates due to thermodynamic instability—similar to

Al_2O_3 nanoparticles. The high surface energy of smaller nanoparticles drives agglomeration to minimize total surface area, leading to non-uniform filling. Although 500 nm SiO_X nanospheres effectively fill the valleys, their sparse distribution may hinder subsequent SAM and perovskite depositions.

Then, we investigated the anchoring of a commonly-used SAM, 2-(9H-carbazol-9-yl)ethyl) phosphonic acid (2PACz), on the SiO_X pre-deposited ITS substrates (named as ITS(SiO_X)/2PACz), together with those on ITS and STS substrates (named as ITS/2PACz and STS/2PACz, respectively), using nano infrared (IR) signals (see Figs. 1c and S5). It is seen that for the ITS/2PACz sample, the 2PACz distribution is highly discontinuous, leading to an uneven potential distribution as revealed by Kelvin probe force microscopy (KPFM) in Fig. 1d. This discontinuity may explain why ITS tandem devices typically require sputtered nickel oxides as a hole selective layer[11–13]. In contrast, the 2PACz exhibits more complete coverage and a more even potential distribution on STS substrates. Notably, after regulating the ITS substrate with SiO_X nanospheres, the 2PACz distribution becomes intact and uniform, resulting in an enhanced homogeneity of contact potential difference. This improved uniformity should reduce the contact loss in an integrated tandem device.

We attributed the non-intact 2PACz coating on the rough ITS substrates with corrugated shapes to the confinement of spaces that facilitates 2PACz molecules to aggregate into clusters[14,24]. The increased depth of these corrugated shapes leads to a smaller initial 2PACz coverage area, as revealed by molecular dynamics simulations in Fig. S6. This is further supported by the 2PACz coverage statistics related to the roughness of ITS substrates filled with varying concentrations of SiO_X (Fig. S7), demonstrating the effectiveness of SiO_X (≥5 mg mL^{-1}) in forming an intact 2PACz layer. We carefully compared the 2PACz distribution under the observations of transmission electron microscopy (TEM) in Fig. S8, which reveals that 2PACz anchors more densely with a substantially connected layer at both the pyramid wall and the SiO_X nanospheres on the ITS(SiO_X) substrate over STS substrate. This enhanced 2PACz coverage is expected to significantly benefit the performance of subsequent tandem devices by improving charge carrier extraction and reducing recombination losses.

Our previous work demonstrated that 2PACz frequently leads to the de-wetting of the overlying perovskite inks, resulting in incomplete coverage of the perovskite layer on STS substrates[25]. This de-wetting issue still exists when utilizing ITS substrates, yet alleviated with SiO_X incorporation, as illustrated in the photographs in Fig. S9. It is also shown that the perovskite precursor contact angel does not increase significantly after depositing SiO_X (Fig. S10), and either no substantial difference in perovskite grain morphology both at the top and buried perovskite surfaces as seen in the SEM image (Figs. 1e and S11). This insignificant correlation between wettability and perovskite grain morphology can be ascribed to the fact that perovskites follow a top-down crystallization mechanism on textured silicon[25]. To trace its impact on perovskite crystallization dynamics, we performed in situ photoluminescence (PL) characterizations to monitor the crystallization process in real-time during spin-coating and subsequent thermal annealing on the two substrates. Fig. S12 presents the time-dependent changes in PL intensity, which exhibits similar PL signals during spin-coating, suggesting comparable nucleation and initial growth processes. However, after annealing, the PL intensity is significantly higher on ITS(SiO_X)/2PACz than on ITS/2PACz, despite that the crystallization rates are about the same, as revealed by the extracted position of the maximum PL intensity at about 175 s. Here, it should be noted that the coverage of hole transport SAM layer on ITS is severely incomplete, while it is almost complete after filling SiO_X, as revealed in Fig. 1c. Therefore, the enhanced PL intensity after annealing is likely due to the prevention of direct contact between ITO and perovskites, implying suppressed nonradiative recombination in perovskite films grown on ITS(SiO_X)/2PACz. This finally leads to the much
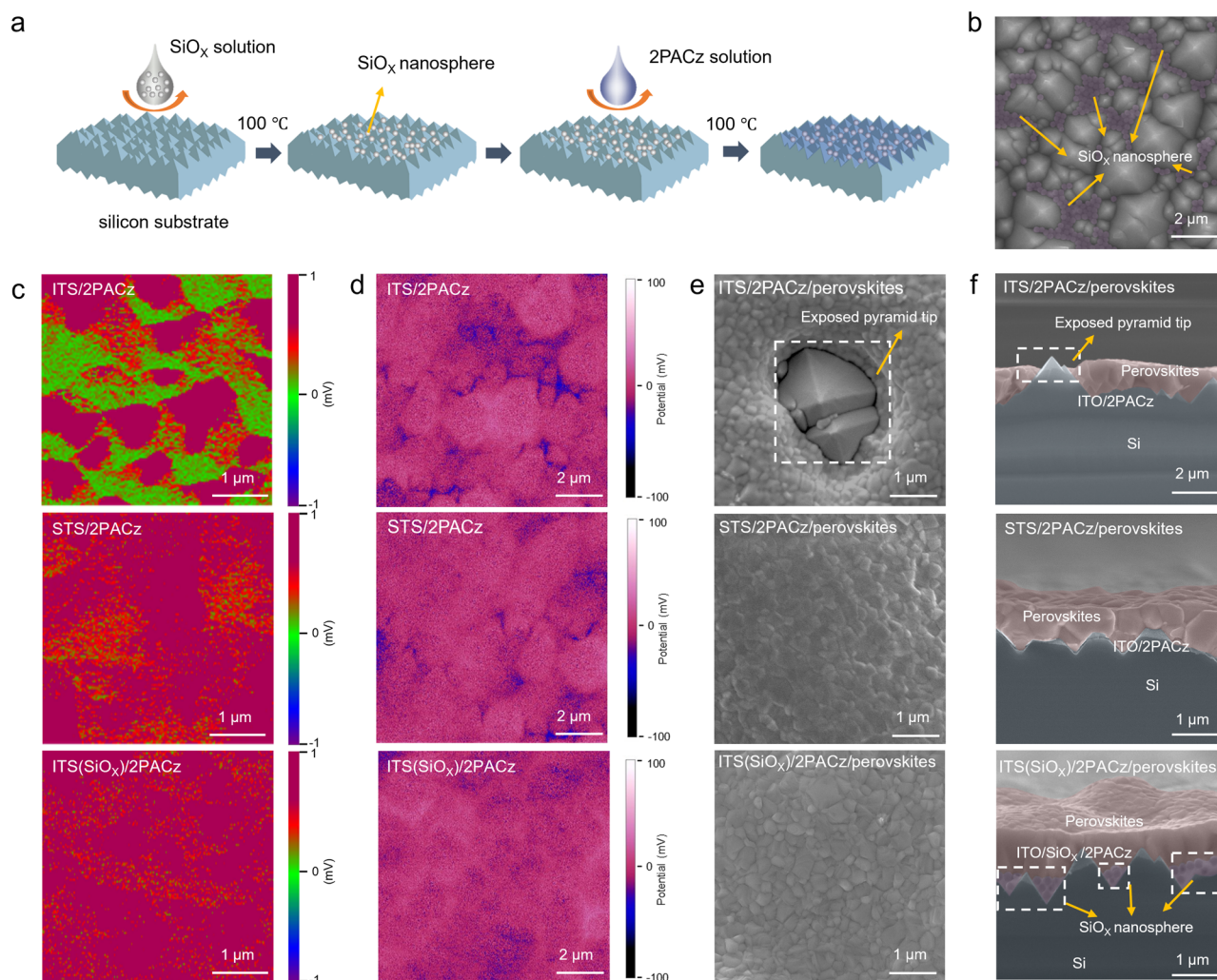
Fig. 1 | Characterization of SAM anchoring and perovskite deposition on textured silicon. a Schematic diagram of the process of 2PACz deposition on ITS with SiO$_X$. **b** SEM surface morphology of SiO$_X$ nanospheres coated on ITS substrates. **c** AFM-IR topographic images corresponding to the 2PACz signal with the IR peak at ~1503 cm^{-1} (Fig. S4) of 2PACz on various textured silicon substrates. **d** Surface potential distributions probed by KPFM of 2PACz on various textured silicon substrates. **e** Surface and **f** cross-sectional SEM morphologies of perovskite deposited on various textured silicon.

more uneven PL intensity distribution of the film on ITS/2PACz compared to that on ITS(SiO$_X$)/2PACz (Fig. S13).

It can be found that the 2PACz-coated substrates still do not maintain the integrity of solution-processed perovskites, as evident from the exposure of pyramid tips in Fig. 1e, f. However, this challenge can be significantly mitigated through the incorporation of SiO$_X$ nanospheres, making ITS surfaces appear as iceberg-like pyramids. Perovskite films deposited on ITS(SiO$_X$) substrates feature localized submicron contacts, exhibiting comparable grain sizes and coverage to those on STS substrates. Additionally, the locally formed insulating SiO$_X$ buffer regions improve the coverage of 2PACz, enabling to achieve efficient monolithic perovskite-silicon tandem solar cells utilizing ITS substrates.

Charge carrier dynamics of localized submicron contacts

To investigate the charge carrier dynamics associated with localized submicron contacts in ITS(SiO$_X$) solar cell devices, we fabricated a perovskite top cell, the structural diagram of which is depicted in Fig. 2a. Cross-sectional electron-beam-induced current (EBIC) measurements (detailed in Supplementary Note 1 and Fig. 2c)[26,27] were conducted to compare the non-equilibrium carrier diffusion and collection capability in the perovskite top cell on ITS(SiO$_X$) with the STS counterpart, whose mapping diagram is shown in Fig. 2b. The EBIC

signal in the whole perovskite top cell on ITS(SiO$_X$) shows notably high intensity, which indicates that the locally contacted top device structure formed on the iceberg-like pyramids of ITS works well as like the top cell on STS.

Additionally, we accessed carrier lifetimes and quantified the recombination losses in perovskite films deposited on both 2PACz-coated silicon substrates (Figs. S14 and S15), confirming that recombination losses are comparable across the two perovskite films. Representative EBIC line-scan profiles from the two perovskite top cells (Fig. 2d) underscore the critical role of C$_{60}$/perovskite heterojunction in facilitating charge carrier collection, demonstrating equivalent carrier-collection capabilities.

To deepen the understanding of carrier transport in perovskites on the 2PACz-coated ITS(SiO$_X$) substrate, we further carried out submicron-zone TRPL measurements. A schematic representation of the measurement system and cross-sectional PL mapping of the perovskite film are shown in Fig. S16. We focused on a single perovskite grain on SiO$_X$, collecting TRPL data away from the laser excitation spot and along the carrier diffusion pathway toward the sidewall of the silicon pyramid. The transiently excited carriers display exponential decay with increasing diffusion distance, yielding a calculated diffusion length (L) of approximately 860 nm (as illustrated in Fig. S17). This diffusion length is critical for understanding the spatial distribution of
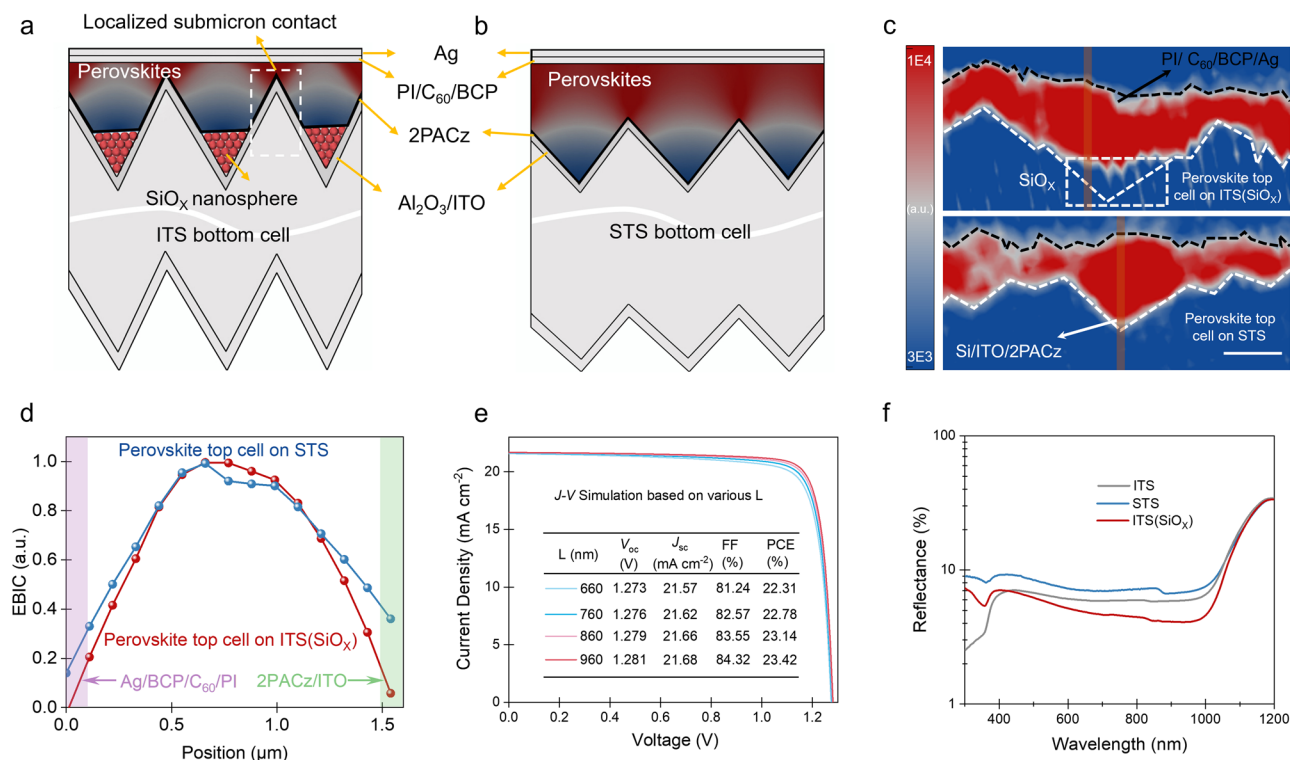
Fig. 2 | Charge carrier dynamics of localized submicron contacts. Schematic description of the perovskite top cells fabricated on **a** ITS(SiOₓ) and **b** STS substrates. The color contrast in perovskite layers represents the strength of the electric field, which corresponds to the simulation results shown in Fig. S13. **c** Cross-section EBIC images of perovskite top cells on ITS(SiOₓ) and STS substrates. The scale bar is 1 μm. **d** Line profiles selected from the EBIC images in the perovskite top solar cell fabricated on ITS(SiOₓ) and STS substrates in this figure (**c**). **e** Simulated J-V curves of the single-junction device with localized submicron contacts varying based on various carrier diffusion lengths. **f** Reflectance of textured silicon substrates.

carriers within the film and their potential contributions to device efficiency.

To validate the extracted L, we simulated the current-voltage (J-V) curves of single-junction perovskite solar cells incorporating localized submicron contacts (as depicted in Fig. 2e, further details provided in Supplementary Note 2). Our simulations revealed that with the increase in L, the photovoltaic performance parameters of the device improve, with fill factor (FF) showing the most significant enhancement, thus supporting the anticipated performance improvements linked to optimized carrier transport characteristics. Furthermore, the simulations of electric field distribution (Figs. 2a and c and S18) reveal that charge carriers predominantly migrate from perovskites toward the pyramid sidewalls (2PACz/ITO) near the pyramid tips on both silicon substrates. In addition, we found that the light trapping of ITS substrates is not significantly affected, yet improves after the presence of SiOₓ at pyramid valleys (Fig. 2f). The antireflection modification of SiOₓ arises from its refractive index[28], which lies between that of air and silicon. As a result, the reflectivity is reduced in accordance with Fresnel's law of reflection[29]. These findings highlight the effectiveness of localized submicron contacts in carrier transport and collection within solar cells.

Improved photoelectric coupling of tandem solar cells

We further examined the impact of SiOₓ incorporation on the optical loss for complete p-i-n tandem configurations based on various silicon substrates, in which the ITS(SiOₓ) tandem structure is showed in Fig. 3a. Reflectance results of silicon substrates in Fig. 2f translate to reduced reflectance losses in ITS(SiOₓ) tandem devices compared to their STS or ITS counterparts (Fig. 3b). These results indicate that the incorporation of SiOₓ nanospheres significantly enhances light trapping within the ITS tandem configuration, thereby improving the

overall efficiency. The underlying mechanism might highlight the role of SiOₓ nanospheres in exciting Mie resonant modes and reducing reflectance losses[30].

Leveraging the enhanced charge carrier transport and reduced interfacial recombination with optimized optical management enabled by localized submicron contacts, we successfully integrated them into monolithic tandem solar cells. Prior optimization reveals a strong correlation between SiOₓ filling depth and tandem performance (Figs. 3c and S19). Low SiOₓ concentrations (≤3 mg mL⁻¹) lead to poor reproducibility and significant V_{OC} deficits due to the presence of shunts from incomplete 2PACz or perovskite coverage as revealed in Figs. 1c–f and S20a. Conversely, high concentrations (7 mg mL⁻¹) result in excessive SiOₓ overfilling (Fig. S20c) and a substantial drop in J_{SC}. Ultimately, 5 mg mL⁻¹ of SiOₓ emerges as the optimal concentration, yielding tandem solar cells with high performance and good reproducibility.

Significantly, ITS(SiOₓ) tandem devices demonstrate a 32.2% average PCE, surpassing the 31.8% average efficiency of STS tandems (Fig. 3c). This enhancement is primarily attributed to the increased J_{SC}, a consequence of maintained light trapping confirmed by optical analysis (Fig. 3b). Additionally, the slightly improved V_{OC} and FF indicate reduced interfacial nonradiative recombination, as evidenced by a bit more homogeneous 2PACz coverage[31,32] in Fig. 1d. However, the two structured tandems show much better performance and reproducibility over ITS tandems without SiOₓ. Conversely, the best laboratory ITS(SiOₓ) tandem solar cell achieves a competitive PCE of 32.57% under reverse scan, compared to 32.11% for the corresponding STS tandem solar cell (Fig. 3d). This performance is accompanied by a J_{SC} of 20.66 mA cm⁻², a V_{OC} of 1.955 V, and an FF of 80.67%.

The integrated J_{SC} obtained from the external quantum efficiency (EQE) spectra (Fig. 3e) reveals a 20.76 mA cm⁻² J_{SC} of the perovskite
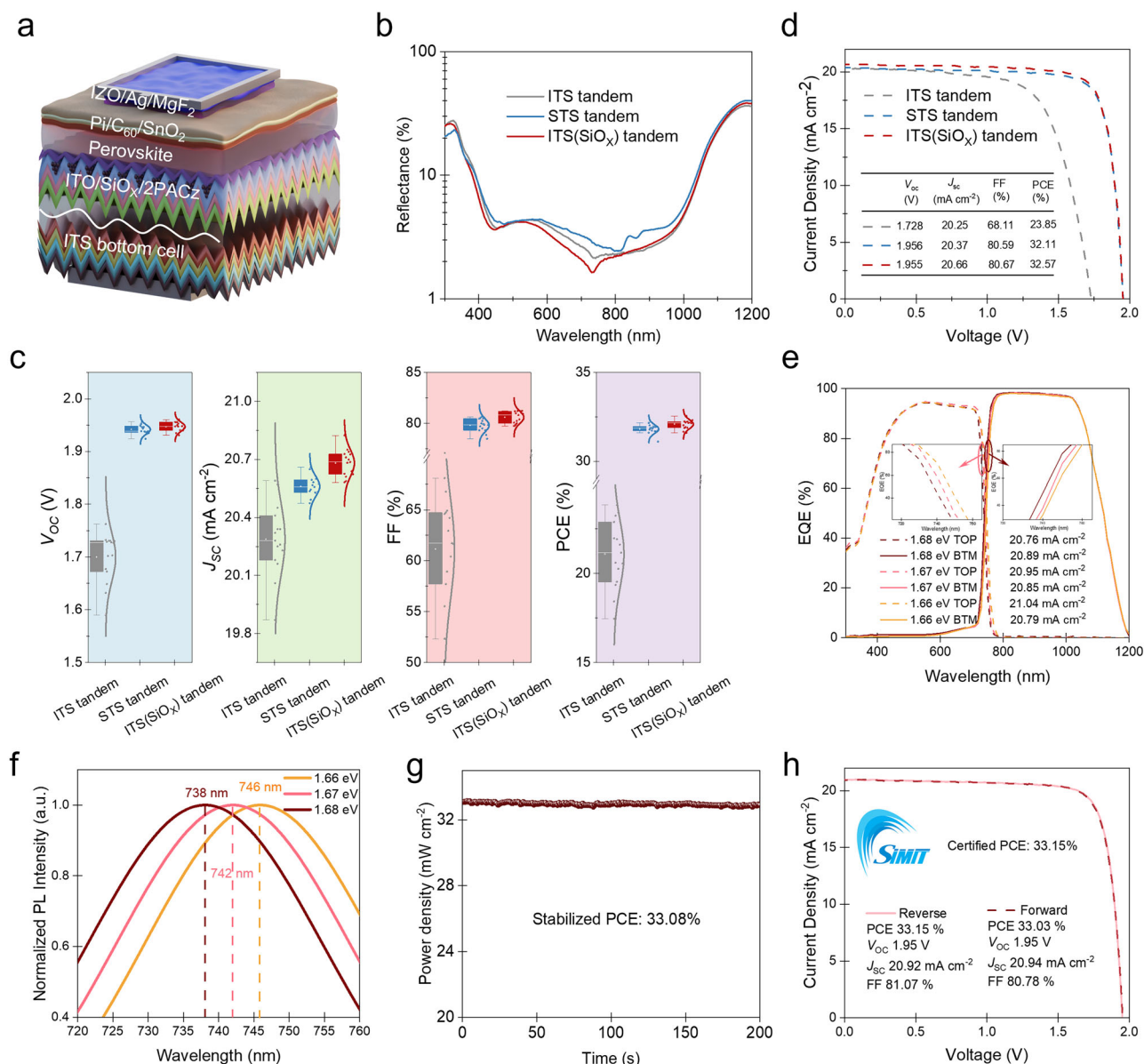
Fig. 3 | Tandem performance with photoelectric regulation. a A schematic structure of monolithic perovskite-silicon tandem solar cells. **b** Evaluation of reflection loss for tandem solar cells with various textured silicon configurations. **c** Statistical charts showing ITS, STS, and ITS(SiO$_X$) tandem performance with 1.68 eV perovskites. **d** The representative *J-V* curves of ITS, STS, and ITS(SiO$_X$) tandems with 1.68 eV perovskites. **e** EQE spectra of tandem solar cells with different perovskite bandgaps (1.66, 1.67, and 1.68 eV) determined by **f** PL peak positions. TOP: perovskite top subcell, BTM: silicon bottom subcell. **g** The steady-state PCE for the best tandem device. **h** The certified PCE for the best tandem device.

sub-cell, which is significantly higher than the tandem without SiO$_X$ (Fig. S21). It can be found that the main photocurrent gain stems from the EQE enhancement ranges during 400–700 nm wavelength, which corresponds well to the light reflection reduction via SiO$_X$ filling as shown in Fig. 3b. However, a higher J_{SC} of 20.89 mA cm^{-2} for the silicon sub-cell was found, compared to the perovskite sub-cell. This motivated us to access a more distant photoelectric coupling of the tandem device via perovskite bandgap tuning, since that a current mismatch in a perovskite-silicon tandem solar cell can significantly affect the device FF[33–35]. We intentionally reduced the bromide ratio in the perovskite to achieve a narrowed bandgap. The PL results in Fig. 3f show a bandgap range of 1.68–1.66 eV for perovskite compositions with bromide content varying from 0.75 to 0.7 (details provided in the Experimental Section). Notably, the corresponding SEM images and X-ray diffraction (XRD) patterns indicate comparable grain sizes and crystallinity for perovskites across this bandgap range (Fig. S22).

Typical EQE spectra in Fig. 3e demonstrate an enhanced integrated J_{SC} for perovskite top cells with narrowed bandgaps. While this strategy result in some sacrifice of the silicon sub-cell's J_{SC}, the overall tandem current limit increased. Combined with improved V_{OC} and FF, tandems employing the 1.67 eV perovskites achieved optimum PCEs, primarily driven by J_{SC} and FF improvements (Fig. S23). The combined effects of localized submicron contacts and perovskite bandgap regulation enabled us to achieve a steady-state efficiency of 33.08% (Fig. 3g), with a certified PCE of 33.15% (Figs. 3h and S24). This represents the highest efficiency reported to date for monolithic perovskite/silicon tandem solar cells with ITS.

Improved stability of tandem solar cells

It is demonstrated that perovskites deposited on textured silicon substrates exhibit downward growth[25,36], with those located in the pyramid valleys being the last to crystallize. This delayed
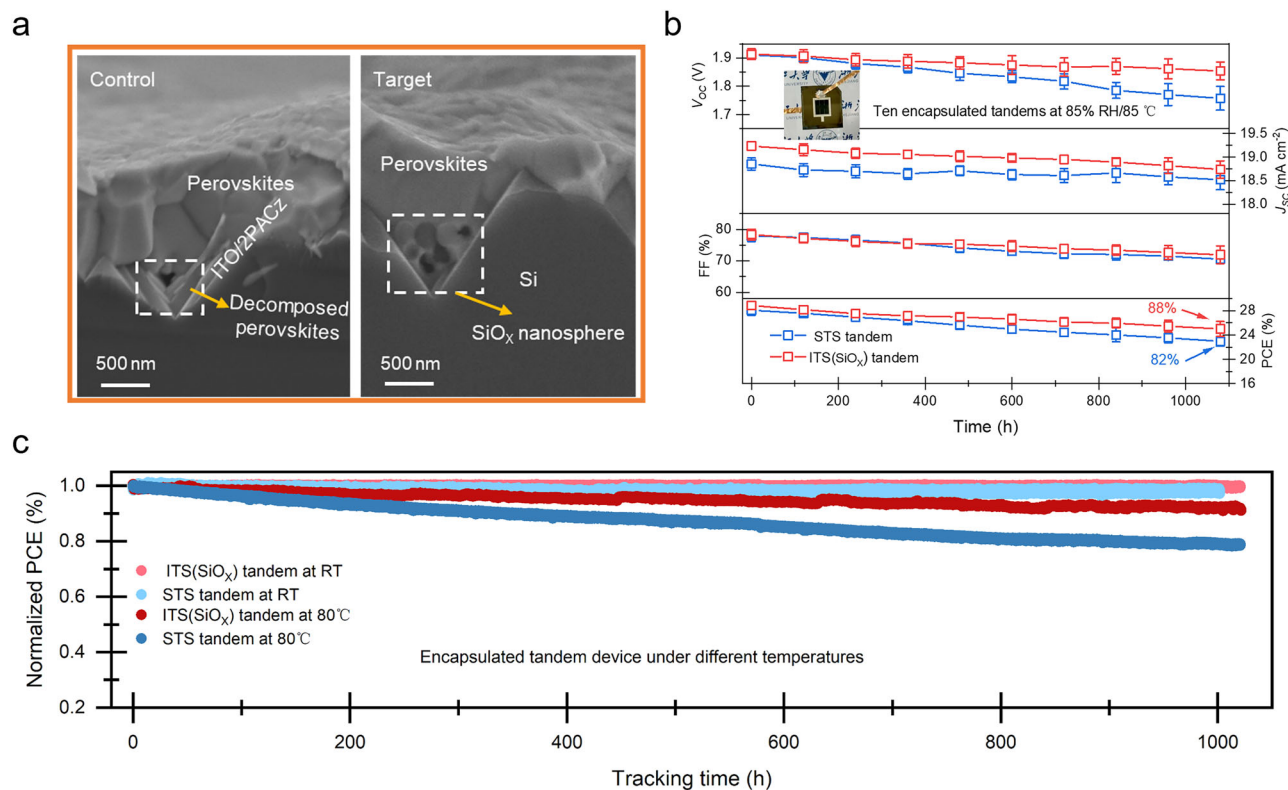
Fig. 4 | Stability of tandem devices. a Cross-sectional SEM images of perovskites on STS substrates, named as control, and ITS (SiO$_X$) substrates, named as target after heat treatments. **b** Ten STS and ITS(SiO$_X$) tandem devices aged under 85% RH/ 85 °C with photovoltaic parameters shown. The inset image is the photograph of an encapsulated tandem device. **c** The MPPT tracking of encapsulated tandem devices at different temperatures in N$_2$.

crystallization thermodynamically leads to a higher density of defects in these regions. At the cutoff areas, the limited availability of sites for the incorporation of perovskite components can result in incomplete integration, giving rise to defects such as vacancies or interstitials[37,38]. These defects may compromise the integrity of the perovskite structure, particularly under thermal stress[15,39], which can negatively impact charge carrier behavior and thereby device stability. To investigate this, we conducted an accelerated aging test by subjecting the samples (perovskites on 2PACz-coated STS, named as control; perovskites on 2PACz-coated ITS, named as target) to 80 °C in N$_2$ for 7 days. SEM analysis (Fig. 4a) revealed preferential decomposition of perovskites at pyramid valleys, indicating increased defects in these regions. Characterization of peeled-off perovskites shows no significant variations in the initial stage (Figs. S25 and S26). However, after thermal treatment, decomposed perovskites and small voids appear at the buried perovskite surface of pyramid valleys peeled off from STS (Fig. S27). XRD analysis reveal that the control perovskites become poorly crystallized and partially decomposed into PbI$_2$, while the target perovskites behave with great structure rigidity. Furthermore, X-ray photoelectron spectroscopy (XPS) reveal decrease in methylamine content (MA, indicated by N 1 s at around 401.8 eV)[40] from 14.27% to 11.61% in control perovskites after heat treatment, while the target perovskites show minimal reduction (Fig. S28), indicative of perovskite decomposition. We further performed comprehensive PL characterization, including steady-state PL, TRPL decay measurements, and spatially resolved PL mapping (Fig. S29). The PL measurements, conducted with laser excitation through the buried interface. It is found that the control film exhibits weak and spatially inhomogeneous PL emission with shorter carrier lifetimes, indicating severer recombination at the buried surface. It also shows a 5 nm spectral shift, clear evidence of phase segregation and mobile ion migration. In striking contrast, the target film

demonstrates significantly stronger and more uniform PL emission, longer carrier lifetimes, and suppressed phase segregation effects.

The presence of SiO$_X$ largely overcomes the geometric limitations at pyramid valleys, reinforcing the 2PACz/perovskite interface. Operational long-term stability of the resulting tandem solar cells was evaluated based on the International Summit on Organic Photovoltaic Stability (ISOS) protocols[41]. All cells were encapsulated with glass packing by UV curing adhesive (inset, Fig. 4b). The sealed adhesive and glass reduce the absorbed light, causing a device J_{SC} loss of about 20% (Fig. S30). Ten STS and ITS(SiO$_X$) tandems were subjected to testing under conditions of relative humidity (RH) 85%/85 °C conditions (ISOS D-3) for 1100 h. The STS tandems exhibit a decrease in average efficiency from 28.08% to 22.95%, maintaining 81.8% of their initial PCEs after 1100 h. In contrast, the ITS(SiO$_X$) tandems demonstrate significant improvement, retaining 86.7% of their initial PCE, which decrease from an average of 28.84% to 24.99%. The major enhancements are observed in V_{OC} and FF, induced by buried interface damage of perovskites, as evidenced by SEM, XRD, and XPS characterizations.

More importantly, MPPT was performed for four representative tandems under 1-sun illumination (the applied light spectrum is shown in Fig. S31) at various temperatures (room temperature or 80 °C) in N$_2$ (ISOS L-1I and 2I; Fig. 4c). The ITS(SiO$_X$) tandem at room temperature maintains its initial efficiency after 1000 h of tracking, while the STS tandem experiences only a minor drop in efficiency. However, under the more rigorous conditions of 80 °C[41,42], the ITS(SiO$_X$) tandem sustains 91.7% of its initial efficiency after 1000 h, significantly outperforming the STS tandem counterpart, which retains only 78.4%. This indicates that the SiO$_X$ incorporation provides enhanced heat resistance. Notably, our tandem devices show stability results compared to those reported in existing literatures (Fig. S32).

Discussion

Our strategy harnesses localized submicron contacts facilitated by SiO_x nanospheres to create an tandem architecture. This approach allows for the formation of a SAM layer, followed by the integration of solution-processed perovskites on ITS substrates. The resulting devices exhibit high efficiencies and enhanced stability, positioning them as promising candidates for the commercialization of perovskite-silicon tandem solar cells. This research paves the way for further exploration and advancements in this dynamic field.

Methods

Materials

All the solvents and reagents were purchased and used directly without further purification. Lead iodide (PbI_2, 99.99%), Cesium iodide (CsI, 99.99%), and [2-(9H-carbazol-9-yl)ethyl]phosphonic acid (2PACz) were purchased from TCI. Formamidinium iodide (FAI, 99.9%), methylammonium bromide (MABr, 99.5%), lead bromide ($PbBr_2$, 99.99%), Piperazinium iodide (PI) and C_{60} (~ 99.9% purity) were all purchased from Xi'an Yuri Solar Co., Ltd. ITO (In_2O_3/SnO_2: 90/10 wt%, 99.99%) and zinc-doped indium oxide (IZO, In_2O_3/ZnO: 90/10 wt%, 99.99%) were purchased from ZhongNuo Advanced Material Technology Co., Ltd. Magnesium fluoride (MgF_2, 99.99%) were purchased from Hebei Luohong Technology Co., Ltd. Tetrakis(dimethylamino) tin(IV) (TDMASn) (99.99%) as one precursor of SnO_2 was purchased from Nanjing Ai Mou Yuan Scientific Equipment Co., Ltd. Ethanol was purchased from Shanghai Aladdin Biochemical Technology Co., Ltd. Anhydrous dimethylformamide (DMF, anhydrous, 99.9%), anhydrous dimethyl sulfoxide (DMSO, anhydrous, ≥99.9%), anhydrous chlorobenzene (anhydrous, 99.9%), and isopropanol (anhydrous, 99.9%) were purchased from Sigma-Aldrich. Mesoporous Silica Nanospheres (200–300 nm, in water) were purchased from Nanjing Jike Biotechnology Co., Ltd and diluted to different concentrations before they were applied to solar cell fabrication.

Silicon heterojunction bottom-cell fabrication

N-type Czochralski (Cz) silicon wafers, with a resistivity of 1–2 Ω.cm and a thickness of 150 μm, were used to fabricate the silicon bottom cell. A slight etching step was first conducted to remove the surface saw damage, and then double-sided random pyramid texture was obtained by a standard texture procedure, resulting in an average-pyramid-height distribution of less than 1.5 μm on both sides. Following a standard RCA cleaning process, the wafers were dipped in buffered HF solution. Subsequently, samples were transferred to a plasma-enhanced chemical vapor deposition (PECVD) cluster (Applied Materials) for deposition of surface passivation stacks. Hydrogenated intrinsic amorphous (i-a-Si:H) layers with a thickness of approximately 5 and 9 nm was grown on front sides and rear side of the pyramid texture wafers, respectively. N-type nanocrystalline silicon oxide (nc-SiO_x:H) and p-type nc-Si:H layers with thicknesses of about 15 and about 12 nm were deposited on the front and back side, respectively. To complete the silicon bottom cell fabrication, a 15 nm thick TCO film was deposited on the front side, and a 75 nm thick transparent conductive oxide (TCO) was deposited on the rear side, followed by screen printing Ag. The front and rear TCO layers have an area of 1.08×1.08 cm^2. The silicon bottom cells were then laser-cut to 3.0×3.0 cm^2 square substrate for tandem fabrication.

Perovskite top cell fabrication

The Si bottom cells were cleaned under UV-ozone for 10 min. For SiO_x-filled Si bottom cells, SiO_x solutions with concentrations of 1 mg mL^{-1}, 3 mg mL^{-1}, 5 mg mL^{-1}, and 7 mg mL^{-1} were spin-coated onto the Si bottom cells at 1500 rpm for 30 s, followed by annealing at 120 °C for 10 min under ambient conditions. The Si bottom cells were subsequently transferred to a nitrogen-filled glovebox for further

processing. The hole transport layer (HTL) was fabricated by spin-coating the 2PACz (1 mg mL^{-1} in ethyl alcohol) at 5000 rpm for 30 s, followed by thermal annealing at 100 °C for 10 min. For the 1.68-eV composition $Cs_{0.05}FA_{0.8}MA_{0.15}PbI_{2.25}Br_{0.75}$, 1.67-eV composition $Cs_{0.05}A_{0.8}MA_{0.15}PbI_{2.27}Br_{0.73}$, 1.66-eV composition $Cs_{0.05}FA_{0.8}MA_{0.15}PbI_{2.29}Br_{0.71}$, 1.75 M perovskite precursor solution was prepared by mixing FAI, MABr, CsI, $PbBr_2$, PbI_2 in DMF: DMSO = 4:1(V/V) mixed solvent subject to the stochiometric ratio. The perovskite precursor (100 μL) was spin-coated at 1750 rpm for 50 s (5 s acceleration to 1750 rpm), subsequently at 5000 rpm for 10 s (1 s acceleration to 5000 rpm). Chlorobenzene (250 μL) was dropped on the film at 10 s before the end of the spinning. The film was immediately annealed at 100 °C for 20 min. Subsequently, 70 μL 0.3 mg mL^{-1} PI was spin-coated onto the perovskite film at a spinning rate of 5000 rpm for 30 s and annealed at 100 °C for 10 min. For the electron transport layer, 10 nm C_{60} was evaporated with a deposition rate of 0.2 Å s^{-1}.

A buffer layer of ~12 nm of SnO_2 was deposited on C_{60} by atomic layer deposition using a PE ALD-F50R (KE-MICRO) system set to 90 °C using 100 cycles of TDMASn source (80 °C, 90 sccm, 1 s pulse, 6.0 s purge) and H_2O (90 sccm, 1 s pulse, 6.0 s purge). Indium zinc oxide (IZO) was then sputtered on top of the SnO_2 through a shadow mask (sheet resistance of 140 Ω/sq, thickness of 40 nm on flat glass). Finally, 500 nm silver electrode at a rate of 1 Å s^{-1}, 110 nm MgF_2 at a rate of 1 Å s^{-1} were thermally evaporated, respectively, under high vacuum.

Device preparation for EBIC testing

To prevent electrical probing-induced device activation, a 100 nm Al_2O_3 insulating layer was deposited via magnetron sputtering on silicon substrates. Deposition occurred at 300 °C under 0.5 Pa Ar atmosphere with 300 W power for 5 h, followed by ambient-air annealing at 550 °C for 2 h to achieve densification. Subsequently, 150 nm indium zinc oxide (IZO) electrodes were patterned through a shadow mask. Then, the silicon substrates underwent UV-ozone cleaning for 10 min. A 5 mg mL^{-1} SiO_x solution was spin-coated at 1500 rpm for 30 s and annealed at 120 °C for 10 min (ambient conditions), then transferred to a nitrogen glovebox. The HTL was formed by spin-coating 2PACz (1 mg mL^{-1} in ethanol) at 5000 rpm for 30 s, followed by 100 °C annealing for 10 min. A 1.75 M perovskite precursor ($Cs_{0.05}A_{0.8}MA_{0.15}PbI_{2.27}Br_{0.73}$) was prepared in DMF: DMSO (4:1 v/v). Precursor solution (100 μL) was spin-coated using a two-step protocol: 1750 rpm for 50 s (5 s acceleration), then 5000 rpm for 10 s (1 s acceleration), with 250 μL chlorobenzene antisolvent dispensed 10 s prior to cycle completion. Films were annealed at 100 °C for 20 min. A PI interlayer (0.3 mg mL^{-1}, 70 μL) was then spin-coated at 5000 rpm for 30 s and annealed (100 °C, 10 min). Finally, 20 nm C_{60}, 6 nm BCP, and 100 nm Ag were thermally evaporated at 0.5 Å^{-1}, 0.5 Å s^{-1}, and 1 Å s^{-1}.

Material characterizations

Molecular dynamics simulations. The density functional theory (DFT) calculations were carried out with the VASP code. The Perdew–Burke–Ernzerhof functional within generalized gradient approximation was used to process the exchange–correlation, while the projector augmented-wave pseudopotential was applied with a kinetic energy cut-off of 500 eV, which was utilized to describe the expansion of the electronic eigenfunctions. The vacuum thickness was set to be 20 Å to minimize interlayer interactions. The Brillouin-zone integration was sampled by a Γ-centered $10 \times 10 \times 1$ Monkhorst–Pack k-point. All atomic positions were fully relaxed until energy and force reached a tolerance of 1×10^{-5} eV and 0.03 eV/Å, respectively. The dispersion corrected DFT-D method was employed to consider the long-range interactions.

Device model and simulation. As illustrated in Fig. S26, the 2D perovskite models based on the substrate of ITS and STS are simplified

from the SEM pictures. The 2D models demonstrates a symmetric characteristic and therefore the simulation is performed on the model based on one textured structure with perovskite covered. We consider the SAMs anchored on ITO can be equivalent to a HTL in terms of function, with electron transport layer (ETL) similarly. The 2D perovskite models were established in COMSOL Multiphysics v6.2 and simulated by resolving the conventional drift-diffusion equations described in previous reports. To ensure that no tunneling or electrical injection occurs through the dielectric layer, we set an insulating boundary condition for these 2D models. The simulation parameters of these models are summarized in Table S1–S3 which is consistent with the good performance of our device. Then, the electric field intensity can be obtained from the carrier concentration distribution in balance when there is no external voltage.

XRD/XPS/SEM/PL. The XRD patterns of perovskite were acquired using a D8 Discover X-ray diffractometer (Bruker) equipped with Cu Kα radiation. The morphology of perovskite was observed using a Hitachi S4800 (Hitachi) Field-Emission Scanning Electron Microscope. XPS characterization was performed using a Kratos AXIS Supra X-ray photoelectron spectrometer with monochromatic Al Kα X-ray (1486.6 eV). Steady-state PL measurements were conducted using an FLS980 spectrometer, equipped with a 470 nm diode laser and a 600 nm long-pass filter. Emission spectra were collected for wavelengths ranging from 600 nm to 850 nm.

TEM. TEM Samples Preparation. The all cross-sectional perovskite solar cells samples were prepared using focus ions beam technique in FEI Helios G4 system. The protecting layer of Pt and amorphous carbon were first deposited, and then the samples were thinned in the subsequent process. The low-voltage thinning at 5 kV and relatively thick sample (~150 nm) was conducted in order to reduce sample damage sustained by ion beam. Finally, the surface damage and contaminations were diminished by a precision polishing at 2 kV. As for the in situ heating process, the prepared thinning lamellae was transferred to the heating chips (Wildfire S3 Nano-chip, DENSsolution) loaded into a heating holder (DENSsolution, SH70).

(S)TEM characterization: The ADF/BF-STEM images and STEM-EDX mapping characterizations were mainly processed in a probe spherical aberration-corrected scanning TEM (FEI-Titan ChemiSTEM G2) operated at 200 kV. The elements analysis was captured in the STEM via the EDX software. In situ heating experiments was performed using DENS solution heating holder with orderly and continuous thermal process operated by the programming controller, and the corresponding STEM images were captured during the heating process.

AFM-IR. AFM-IR analysis was performed by an Infrared Scanning Near-field Optical Microscopy (Anasys nanoIR2-s). Both height and chemical images were obtained in contact mode using a Contact Mode AFM Probe for nanoIR2-s in an ambient atmosphere.

KPFM measurements. KPFM measurements were performed in PeakForce tapping mode on a the Bruker Dimension Icon using scm-pit-v2 probes(0.01–0.025 Ω·cm, Antimony (n) doped Si). The measurements were performed under AM-KPFM with 75 KHz resonant frequency, 3.0 N/m Spring Constant, 25 nm tip radius.

TRPL mapping and line scan TRPL measurements. TPLM and Line Scan TRPL were measured by using the PicoQuant Micro Time 100 confocal microscopic system. An Olympus 100× oil immersion objective with a numerical aperture of 1.45 was used for the measurement. Samples were covered by immersion oil (Olympus Immersion Oil Type-F) in a dark environment during the measurement. Picosecond 640 nm pulsed laser with a repetition rate of 5 MHz was used to measure the cross-sectional PL Mapping of perovskite films with composition of $Cs_{0.05}A_{0.8}MA_{0.15}PbI_{2.25}Br_{0.75}$. The average laser intensity was kept at around 12 nW at the repetition rate of 5 MHz, corresponding to a photon energy of ~ 2.4 fJ per pulse. For the Line Scan TRPL measurement, the 640 nm laser was fixed on the top of perovskite grains and the signal of a series of selected points along the line from the top to the bottom or the side of the grain were collected by time-correlated single-photon counting modules (TimeHarp 260). The integration time for each point is 120 s and the minimum temporal resolution was 1.6 ns. The repetition rate of 640 nm laser was set at 0.2 MHz for the TRPL measurement to ensure that the complete decay of the fluorescence signal.

EBIC measurements. EBIC and the cross-section SEM data was acquired through HITACH S-3400N, Gatan DIGISCAN II and low-noise current preamplifier (SRS Model SR570). The accelerating voltage of 5 kV with a probe current of 50 pA. The cross-section EBIC sample was prepared by mechanically cracking the fabricated devices.

Device measurements. The current density–voltage (J–V) curves were determined using a Keithley 2400 source measurement unit under a simulated AM 1.5 G spectrum with a Newport 94022 A solar simulator. The light intensity was calibrated by a standard Si reference solar cell (PVM937, Newport) with KG5 filter calibrated by Newport Corporation TAC-PV Lab. The spectral mismatch correction factor is M = 0.994 ± 0.001. The J–V curves of devices were measured both in reverse scan (2 V to −0.1 V with a step of 0.013 V and a dwelling time of 10 ms at each step) and forward scan (−0.1 V to 2 V with a step of 0.013 V and a dwelling time of 10 ms at each step). The device was tested at room temperature (25 ± 5 °C) with a relative humidity of 30 ± 10% under ambient conditions. All devices were measured without pre-conditioning, such as light-soaking the device. The device was tested with a calibrated mask with an aperture area of 1 cm^2. The steady-state PCE was calculated by measuring the stabilized photocurrent density under a constant bias voltage. EQE curves were measured using an EQE measurement system (Model QEX10, PV Measurements, Inc.). The chopped monochromatic light beam was fully focused on the active area of the tandems. For perovskite top cell measurement, the silicon bottom cells were saturated by an infrared light-bias LED with 850 nm peak emission. A bias voltage of 0.6 V was used to realize the almost short-circuit conditions. When measuring the silicon bottom cells, a blue light-bias LED with 455 nm peak emission was used to saturated the perovskite subcells and a 1 V bias voltage was applied to maintain the short circuit conditions.

Device encapsulation. The front and back electrodes of the tandem devices were dot-coated with Ag paste to ensure proper contact with conductive copper tapes, which extended beyond the sealed region and served as electrodes for stability testing. The tandems were then sandwiched between two polished glass substrates, each 1.1 mm thick, and sealed along the edges with epoxy, taking care to avoid any contact with the active devices.

Stability tests. For maximum power point (MPP) tracking, the encapsulated devices were tested in ambient air under continuous illumination from a Xenon lamp-based solar simulator (Enli Tech, SS-F5-3A), calibrated to a light intensity of 100 mW cm^{-2}. The illuminated area was defined by a 1 cm² shadow mask.

For damp-heat testing (85% RH/85 °C), the sealed devices were aged on a hotplate at 85 °C with ambient humidity controlled at 85% RH, using an ultrasonic humidifier with adjustable settings. During J-V measurements, the tandem devices were transferred to a separate room maintained at <30% RH and room temperature, and returned to the aging environment immediately after testing.

Reporting summary

Further information on research design is available in the Nature Portfolio Reporting Summary linked to this article.

Data availability

The main data supporting the findings of this study are available in the main text, the Supplementary Information, and the Source Data file. All other data of this work are available from the corresponding authors on request. Source data are provided with this paper.

References

1. Green, M. A. et al. Solar cell efficiency tables (Version 64). *Prog. Photovolt. Res. Appl.* **32**, 425–441 (2024).
2. Shockley, W. & Queisser, H. J. Detailed balance limit of efficiency of *p-n* junction solar Cells. *J. Appl. Phys.* **32**, 510–519 (1961).
3. Futscher, M. H. & Ehrler, B. Efficiency limit of perovskite/Si tandem solar cells. *ACS Energy Lett.* **1**, 863–868 (2016).
4. Li, Z. et al. Cost analysis of perovskite tandem photovoltaics. *Joule* **2**, 1559–1572 (2018).
5. Mariotti, S. et al. Interface engineering for high-performance, triple-halide perovskite–silicon tandem solar cells. *Science* **381**, 63–69 (2023).
6. Aydin, E. et al. Enhanced optoelectronic coupling for perovskite/silicon tandem solar cells. *Nature* **623**, 732–738 (2023).
7. Ugur, E. et al. Enhanced cation interaction in perovskites for efficient tandem solar cells with silicon. *Science* **385**, 533–538 (2024).
8. Liu, J. et al. Perovskite-silicon tandem solar cells with bilayer interface passivation. *Nature* **635**, 596–603 (2024)
9. Hou, Y. et al. Efficient tandem solar cells with solution-processed perovskite on textured crystalline silicon. *Science* **367**, 1135–1140 (2020).
10. Chin, X. Y. et al. Interface passivation for 31.25%-efficient perovskite/silicon tandem solar cells. *Science* **381**, 59–63 (2023).
11. Luo, X. et al. Efficient perovskite/silicon tandem solar cells on industrially compatible textured silicon. *Adv. Mater.* **35**, 2207883 (2023).
12. Li, C. et al. Enhancing efficiency of industrially-compatible monolithic perovskite/silicon tandem solar cells with dually-mixed self-assembled monolayers. *Adv. Funct. Mater.* **34**, 2407805 (2024).
13. Mao, L. et al. Fully textured, production-line compatible monolithic perovskite/silicon tandem solar cells approaching 29% efficiency. *Adv. Mater.* **34**, 2206193 (2022).
14. Park, S. M. et al. Low-loss contacts on textured substrates for inverted perovskite solar cells. *Nature* **624**, 289–294 (2023).
15. Tang, H. et al. Reinforcing self-assembly of hole transport molecules for stable inverted perovskite solar cells. *Science* **383**, 1236–1240 (2024).
16. Sahli, F. et al. Fully textured monolithic perovskite/silicon tandem solar cells with 25.2% power conversion efficiency. *Nat. Mater.* **17**, 820–826 (2018).
17. Xu, Q. et al. Diffusible capping layer enabled homogeneous crystallization and component distribution of hybrid sequential deposited perovskite. *Adv. Mater.* **36**, 2308692 (2024).
18. Jiao, B. et al. Realizing stable perovskite solar cells with efficiency exceeding 25.6% through crystallization kinetics and spatial orientation regulation. *Adv. Mater.* **36**, 2313673 (2024).
19. Hang, P. et al. Highly efficient and stable wide-bandgap perovskite solar cells via strain management. *Adv. Funct. Mater.* **33**, 2214381 (2023).
20. Peng, W. et al. Reducing nonradiative recombination in perovskite solar cells with a porous insulator contact. *Science* **379**, 683–690 (2023).
21. Peng, J. et al. Nanoscale localized contacts for high fill factors in polymer-passivated perovskite solar cells. *Science* **371**, 390–395 (2021).
22. Guo, R. et al. Refining the substrate surface morphology for achieving efficient inverted perovskite solar cells. *Adv. Energy Mater.* **13**, 2302280 (2023).
23. Shi, P. et al. Strain regulates the photovoltaic performance of thick-film perovskites. *Nat. Commun.* **15**, 2579 (2024).
24. Curcio, E., Curcio, V., Profio, G. D., Fontananova, E. & Drioli, E. Energetics of protein nucleation on rough polymeric surfaces. *J. Phys. Chem. B* **114**, 13650–13655 (2010).
25. Kan, C. et al. Efficient and stable perovskite-silicon tandem solar cells with copper thiocyanate-embedded perovskite on textured silicon. *Nat. Photon.* **19**, 63–70 (2025).
26. Correa-Baena, J.-P. et al. Homogenized halides and alkali cation segregation in alloyed organic-inorganic perovskites. *Science* **363**, 627–631 (2019).
27. Wang, R. et al. Constructive molecular configurations for surface-defect passivation of perovskite photovoltaics. *Science* **366**, 1509–1513 (2019).
28. Mazzarella, L. et al. Infrared photocurrent management in monolithic perovskite/silicon heterojunction tandem solar cells by using a nanocrystalline silicon oxide interlayer. *Opt. Express* **26**, A487 (2018).
29. Wang, S. et al. Anti-reflection effect of high refractive index polyurethane with different light trapping structures on solar cells. *Heliyon* **9**, e20264 (2023).
30. Shameli, M. A., Mirnaziry, S. R. & Yousefi, L. Distributed silicon nanoparticles: an efficient light trapping platform toward ultrathin-film photovoltaics. *Opt. Express* **29**, 28037 (2021).
31. Chen, Y. et al. Nuclei engineering for even halide distribution in stable perovskite/silicon tandem solar cells. *Science* **385**, 554–560 (2024).
32. Liang, Z. et al. Homogenizing out-of-plane cation composition in perovskite solar cells. *Nature* **624**, 557–563 (2023).
33. Boccard, M. & Ballif, C. Influence of the subcell properties on the fill factor of two-terminal perovskite–silicon tandem solar cells. *ACS Energy Lett.* **5**, 1077–1082 (2020).
34. Bowman, A. R. et al. Relaxed current matching requirements in highly luminescent perovskite tandem solar cells and their fundamental efficiency limits. *ACS Energy Lett.* **6**, 612–620 (2021).
35. Tockhorn, P. et al. Nano-optical designs for high-efficiency monolithic perovskite–silicon tandem solar cells. *Nat. Nanotechnol.* **17**, 1214–1221 (2022).
36. Chen, S. et al. Crystallization in one-step solution deposition of perovskite films: upward or downward? *Sci. Adv.* **7**, eabb2412 (2021).
37. Cai, S. et al. Intragrain impurity annihilation for highly efficient and stable perovskite solar cells. *Nat. Commun.* **15**, 2329 (2024).
38. Chen, S. et al. Stabilizing perovskite-substrate interfaces for high-performance perovskite modules. *Science* **373**, 902–907 (2021).
39. Zhao, K. et al. Peri-fused polyaromatic molecular contacts for perovskite solar cells. *Nature* **632**, 301–306 (2024).
40. Park, B. et al. Stabilization of formamidinium lead triiodide α-phase with isopropylammonium chloride for perovskite solar cells. *Nat. Energy* **6**, 419–428 (2021).
41. Khenkin, M. V. et al. Consensus statement for stability assessment and reporting for perovskite photovoltaics based on ISOS procedures. *Nat. Energy* **5**, 35–49 (2020).
42. Yang, Y. et al. Inverted perovskite solar cells with over 2000 h operational stability at 85 °C using fixed charge passivation. *Nat. Energy* **9**, 37–46 (2023).

Author contributions

D.Y.Z. and P.J.H. conceived the idea, designed the experiments, and wrote the original draft. D.Y.Z. fabricated the devices and conducted the *J-V*, EQE, SEM, PL, XPS, XRD, and stability measurements. D.Y.Z. and T.W. contributed to the device fabrication and certification. D.Y.Z., and B.L. contributed to the EBIC measurements and wrote their corresponding portion of the draft. R.L.L. contributed to the simulation calculation. Z.Y.N. and H.Y.Z. contributed to TRPL Mapping and Line Scan TRPL Measurements. D.G.D. contributed to the TEM characterization. C.X.K. and Y.X.Y. contributed to the AFM-IR, PL mapping. J.Y.W. contributed to basic characterization and data processing. Z.G.Y. provided the materials necessary for the preparation of the tandem devices. K.F.Q. and T.W. designed and prepared the silicon bottom cells. X.G.Y., D.R.Y., and P.J.H. provided the funding support. X.G.Y. and P.J.H. revised the manuscript. X.G.Y. and D.R.Y. supervised the experimental development, led the project and reviewed the manuscript. All authors discussed the results and commented on the manuscript.

Competing interests

The authors declare no competing interests.

Additional information

Supplementary information The online version contains supplementary material available at https://doi.org/10.1038/s41467-025-62389-3.

Correspondence and requests for materials should be addressed to Pengjie Hang, Deren Yang or Xuegong Yu.

Peer review information *Nature Communications* thanks Pingqi Gao, Zhanhua Wei, and the other, anonymous, reviewer(s) for their contribution to the peer review of this work. A peer review file is available.

Reprints and permissions information is available at http://www.nature.com/reprints

Publisher's note Springer Nature remains neutral with regard to jurisdictional claims in published maps and institutional affiliations.